Ultrathin MnO_2/Graphene Oxide/Carbon Nanotube Interlayer as Efficient Polysulfide-Trapping Shield for High-Performance Li–S Batteries

*Weibang Kong, Lingjia Yan, Yufeng Luo, Datao Wang, Kaili Jiang, Qunqing Li, Shoushan Fan, and Jiaping Wang**

Ultrathin MnO_2/graphene oxide/carbon nanotube (G/M@CNT) interlayers are developed as efficient polysulfide-trapping shields for high-performance Li–S batteries. A simple layer-by-layer procedure is used to construct a sandwiched vein–membrane interlayer of thickness 2 µm and areal density 0.104 mg cm^{-2} by loading MnO_2 nanoparticles and graphene oxide (GO) sheets on superaligned carbon nanotube films. The G/M@CNT interlayer provides a physical shield against both polysulfide shuttling and chemical adsorption of polysulfides by MnO_2 nanoparticles and GO sheets. The synergetic effect of the G/M@CNT interlayer enables the production of Li–S cells with high sulfur loadings (60–80 wt%), a low capacity decay rate (–0.029% per cycle over 2500 cycles at 1 C), high rate performance (747 mA h g^{-1} at a charge rate of 10 C), and a low self-discharge rate with high capacity retention (93.0% after 20 d rest). Electrochemical impedance spectroscopy, cyclic voltammetry, and scanning electron microscopy observations of the Li anodes after cycling confirm the polysulfide-trapping ability of the G/M@CNT interlayer and show its potential in developing high-performance Li–S batteries.

1. Introduction

The increasing use of portable electronic devices and electric vehicles is resulting in an ever-increasing demand for rechargeable batteries with high energy densities and long service lives. Traditional Li-ion batteries (LIBs) are approaching their theoretical capacity limits.[1,2] Li–S batteries have great potential for use in next-generation energy-storage systems because of their high theoretical capacity (1672 mA h g^{-1}) and energy density (2600 W h kg^{-1}); these are nearly fivefold higher than those of current LIBs.[3,4] In addition, sulfur has the advantages over current cathode materials of natural abundance, nontoxicity, and low cost. Li–S batteries have therefore been extensively researched in recent years. However, Li–S batteries have three drawbacks. First, the low conductivities of sulfur and the discharge products (Li_2S_2/Li_2S) result in poor electrochemical performance of the cell. A higher content of a conductive additive is needed and this reduces the energy density of the electrode. Second, the large volume change of sulfur (≈80%) and aggregation of charge/discharge products during cycling gradually decrease the mechanical integrity and stability of the electrode. Third, and most importantly, internal shuttling of the dissolved intermediate lithium polysulfides between the electrodes results in loss of active materials, i.e., the shuttle effect.[5,6] All these factors cause critical problems, including decreased coulombic efficiencies, rapid capacity decay, and inferior rate performances of Li–S batteries.

In recent decades, various methods have been proposed for solving these problems. The main strategy used to minimize the shuttle effect has been to construct functional cathode architectures that physically or chemically restrain polysulfides dissolution, such as core–shell structures coated with polymeric or carbon materials,[7,8] yolk–shell nanostructures encapsulated by polyaniline or TiO_2 shells,[9,10] layer-by-layer porous carbon structures,[11,12] and structures modified with poly(vinyl pyrrolidine) or poly(ethylene glycol).[13,14] Carbon materials such as porous carbon, carbon nanotubes (CNTs), graphene, and graphene oxides (GOs) have attracted much attention as host materials for sulfur cathodes because of their specific structures and excellent physical and electrochemical properties.[8,11–21] CNTs in particular are extensively used for fabricating highly flexible carbon–sulfur composite cathodes with favorable electrochemical performances.[13,15–21] An interwoven CNT network as the electrode host structure provides a large surface area for adsorbing polysulfides, a porous structure to accommodate volume expansion, and continuous electronic contacts to enhance electron transport. Recently, binder-free S–CNT composites with high stabilities and high rate performances based on superaligned carbon nanotubes (SACNTs) have been developed.[13,17,18] SACNTs have excellent conductivities, large aspect ratios (≈10^4), and can be drawn into thin films because of the strong van der Waals forces among

W. Kong, L. Yan, Y. Luo, D. Wang, Prof. K. Jiang, Prof. Q. Li, Prof. S. Fan, Prof. J. Wang
Department of Physics and Tsinghua-Foxconn Nanotechnology Research Center
Tsinghua University
Beijing 100084, China
E-mail: jpwang@tsinghua.edu.cn
Prof. K. Jiang, Prof. Q. Li, Prof. J. Wang
Collaborative Innovation Center of Quantum Matter
Beijing 100084, China

DOI: 10.1002/adfm.201606663

the tubes and bundles.[22–24] These properties result in the formation of highly conductive, 3D, and flexible CNT network, which promotes the polysulfide-trapping ability and enhances the electrochemical properties of sulfur cathodes. Because they do not need a binder or current collector, S–SACNT composite electrodes are simple to fabricate and have high specific energy densities.

Another strategy for alleviating the shuttle effect is to develop functional separators. The separator is an important battery component; it separates the cathode and anode to avoid inner short circuiting and allows Li-ion transport between the electrodes.[25] Separators are often porous polymer membranes, which can be easily penetrated by dissolved polysulfides. Ideal separators for Li–S batteries should be able to block polysulfide shuttling and tightly confine the active materials in the cathode structure.[5,6,26] Many groups have focused on developing functional separators for Li–S cells.[26–35] Various materials such as Nafion membranes,[28] porous carbon,[29,30] CNTs,[31] GOs,[32] and metal oxides[33] have been used to construct functional interlayers on separators. Chung and Manthiram described a separator coated with a lightweight CNT interlayer for alleviating the shuttle effect.[31] The CNT interlayer acts as both an inner current collector to facilitate electron conduction, and a physical barrier to restrain polysulfides diffusion. However, the relatively open structure of the porous CNT network hardly blocks dissolved polysulfides. It is also difficult for nonpolar CNTs to adsorb polar polysulfides. GOs are effective host materials for restraining polysulfides dissolution, probably because of interactions between the functional oxygen groups and polysulfides.[32,36] Wei and co-workers developed a thin GO-coated separator for alleviating polysulfides diffusion and achieved significant improvements in the discharge capacity and cycling stability.[32] However, further improvements in the active sulfur loading, prolonged cycling stability, and high rate performances are still needed. Long-chain polysulfides are highly polar and soluble, therefore polar materials (metal oxides) or polar oxygen groups have strong chemical interaction with polysulfides.[34,37–40] Li–S cells based on polar materials such as TiO_2,[33] MnO_2,[37–39] and metal–organic frameworks[40] have greatly improved cycling stabilities. Nazar and co-workers confirmed that the oxygen groups from MnO_2 and GO sheets can react with polysulfides to form surface-bound intermediates, i.e., $S_2O_3^{2-}$ species, preventing polysulfides dissolution.[38] However, the low conductivities of these materials adversely affect the redox kinetics of the cell, resulting in poor rate performances and prolonged cycling instability. Also, larger amounts of conductive additives are needed, reducing the energy density and sulfur loading of the cathodes.[5]

Here, we present a functional MnO_2/graphene oxide/carbon nanotube (G/M@CNT) interlayer applied in Li–S batteries, with synergetic effects among the GO sheets, MnO_2 nanoparticles, and SACNT films. The G/M@CNT interlayer had a thickness of ≈2 µm and an areal density of 0.104 mg cm^{-2}, and accounted for only 4 wt% of the electrode. No current collector or polymer binder was used in the cathode structure, and the sulfur content reached 80 wt%. Because of the strong adsorption of polysulfides on the GO sheets and MnO_2 nanoparticles, and the outstanding mechanical properties and conductivity of the SACNT films, the G/M@CNT interlayer effectively prevented polysulfides diffusion, and the sulfur electrodes had excellent cycling stability, with –0.029% decay per cycle for 2500 cycles at 1 C, and a high rate performance of 750 mA h g^{-1} at 10 C. To the best of our knowledge, such a high cycling stability and high rate performance have rarely been reported.

2. Results and Discussion

A schematic diagram of a Li–S battery with the G/M@CNT interlayer is shown in **Figure 1**a. Conventional separators in Li–S cells are often made of porous polypropylene/polyethylene films, which are usually nonpolar. In contrast, the polysulfides generated during charge/discharge processes are highly polar and soluble, therefore a conventional separator can hardly restrain polysulfides diffusion. A functional G/M@CNT interlayer was coated on the separator via a simple layer-by-layer method to solve this problem. Ultrathin and freestanding cross-stacked SACNT films were drawn from SACNT arrays

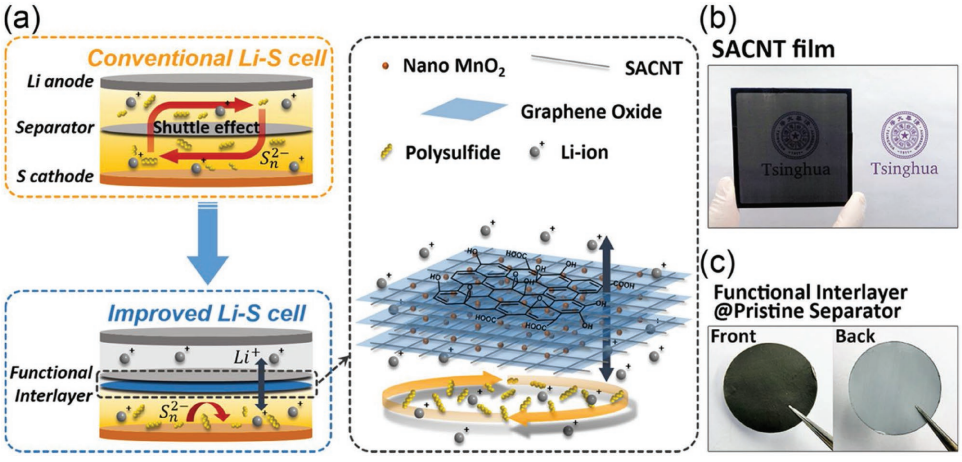

Figure 1. a) Schematic diagram of electrode structure with the functional G/M@CNT interlayer. Photographs of b) SACNT film with five cross-stacked layers and c) G/M@CNT interlayer coated separator.

(Figure 1b). A suspension of well-dispersed MnO_2 nanoparticles anchored on GO sheets in ethanol was obtained by ultrasonication, and then deposited uniformly on the SACNT films. After drying, a vein–membrane film consisting of MnO_2 nanoparticles, GO sheets, and cross-stacked SACNT films was obtained. The procedure was repeated for layer-by-layer construction of a G/M@CNT interlayer. In this study, the G/M@CNT interlayer consisted of 10 layers of hybrid vein–membrane films. Because of the well-dispersed MnO_2/GO layer structure and outstanding mechanical properties of the SACNT films, the G/M@CNT interlayer was ultrathin with a sandwiched vein–membrane structure. Figure 1c shows photographs of the front and back of the G/M@CNT interlayer-coated separator. The functional G/M@CNT interlayer has an open structure for ion transport because of the unique vein–membrane structure. Meanwhile, the G/M@CNT interlayer can improve the polysulfide-trapping ability because of the strong interactions between polysulfides and the oxygen groups in the MnO_2 nanoparticles and GO sheets.

The scanning electron microscopy (SEM) image in **Figure 2**a shows that the pristine separator had a flat surface and many channels throughout the membrane. The pore sizes of the polymer membrane were 200–500 nm, through which dissolved polysulfides of size less than 2 nm can easily pass.[6,26,41] In contrast, the unique vein–membrane structure of the functional G/M@CNT interlayer showed a synergetic effect in the structure that can effectively prevent polysulfide diffusion (Figure 2b–d). The cross-sectional SEM image shows that the thickness of the G/M@CNT interlayer was only 2 µm, and the areal density of the interlayer was only 0.104 mg cm^{-2}. In such ultrathin interlayer, the cross-stacked CNT network acted as the support veins in the functional interlayer (Figure 2b), thus the MnO_2/GO sheets could be uniformly dispersed and sandwiched. GO sheets can not only provide an effective support membrane for MnO_2 dispersion and polysulfide adsorption (Figure S1, Supporting Information) but also cover the open porous structure of the cross-stacked CNT network. Meanwhile, MnO_2 nanoparticles can provide more effective adsorption for polysulfides to further improve the electrochemical performance of Li–S cell. Energy-dispersive X-ray (EDX) spectroscopy mapping (inset of Figure 2c) showed that carbon and manganese were uniformly dispersed on the surface of the G/M@CNT interlayer, indicating a homogeneous distributions of GO sheets and MnO_2 nanoparticles.

Freestanding S–CNT composite electrodes were fabricated via dispersion and codeposition of sulfur particles and oxidized CNTs in water/ethanol solution. The surface of the S–CNT composite electrode shows formation of a continuous CNT network (Figure S2, Supporting Information). Thermogravimetric analysis (TGA; Figure S3, Supporting Information) shows that the sulfur contents of the S–CNT composite electrodes ranged from 60 to 80 wt%, corresponding to areal densities of sulfur from 1.11 to 2.37 mg cm^{-2}. The G/M@CNT functional interlayer accounted for only 4 wt% of the electrode.

Figure 3 shows the electrochemical performances of Li–S cells with the G/M@CNT interlayer and the pristine separator. To examine the effects of the individual components of the G/M@CNT interlayer, cross-stacked SACNT films (CNT interlayer) and GO sheets sandwiched by SACNT films (G@CNT interlayer) were also fabricated, and the electrochemical performances of Li–S cells with separators coated by these interlayers were examined. As shown in Figure 3a, at the same sulfur loading (65 wt%) and galvanostatic charge/discharge rate, i.e., 0.5 C (1 C = 1672 mA g^{-1}), the cycling stability of the Li–S cells was improved significantly by stepwise introduction of a CNT film, GO sheets, and MnO_2 nanoparticles. The synergetic effects of the G/M@CNT interlayer enabled an initial discharge capacity of 1026 mA h g^{-1} to be obtained, and the retention after 200 cycles was ≈82%. In contrast, the cell with the pristine separator showed a lower initial discharge capacity, i.e., 869 mA h g^{-1}, with fast capacity degradation in 200 cycles.

Although MnO_2 nanoparticles can be effective in preventing polysulfide dissolution, they also gave rise to side reaction as an anode material,[42–44] which will affect the coulombic efficiency in Li–S cell. For the G/M@CNT interlayer applied cell, the average coulombic efficiency for 200 cycles at 0.5 C was 98.0%, compared to 98.7% for the cell with the pristine separator (Figure 3b). To examine the effect of MnO_2 particles on coulombic efficiency, sulfur electrodes with G/M@CNT interlayer at high content of MnO_2 (5 wt%) and MnO_2/CNT electrode were fabricated. Figure S4a (Supporting Information) showed the comparison of the cycling performances and coulombic efficiencies of sulfur electrodes

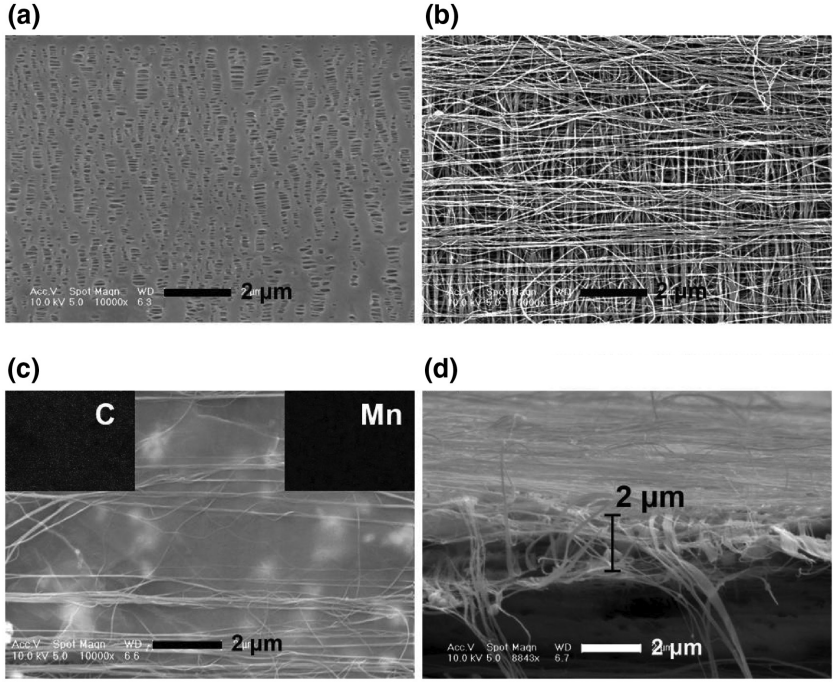

Figure 2. SEM images of a) pristine separator, b) SACNT cross-stacked film, c) top surface, and d) cross-sectional morphology of G/M@CNT interlayer.

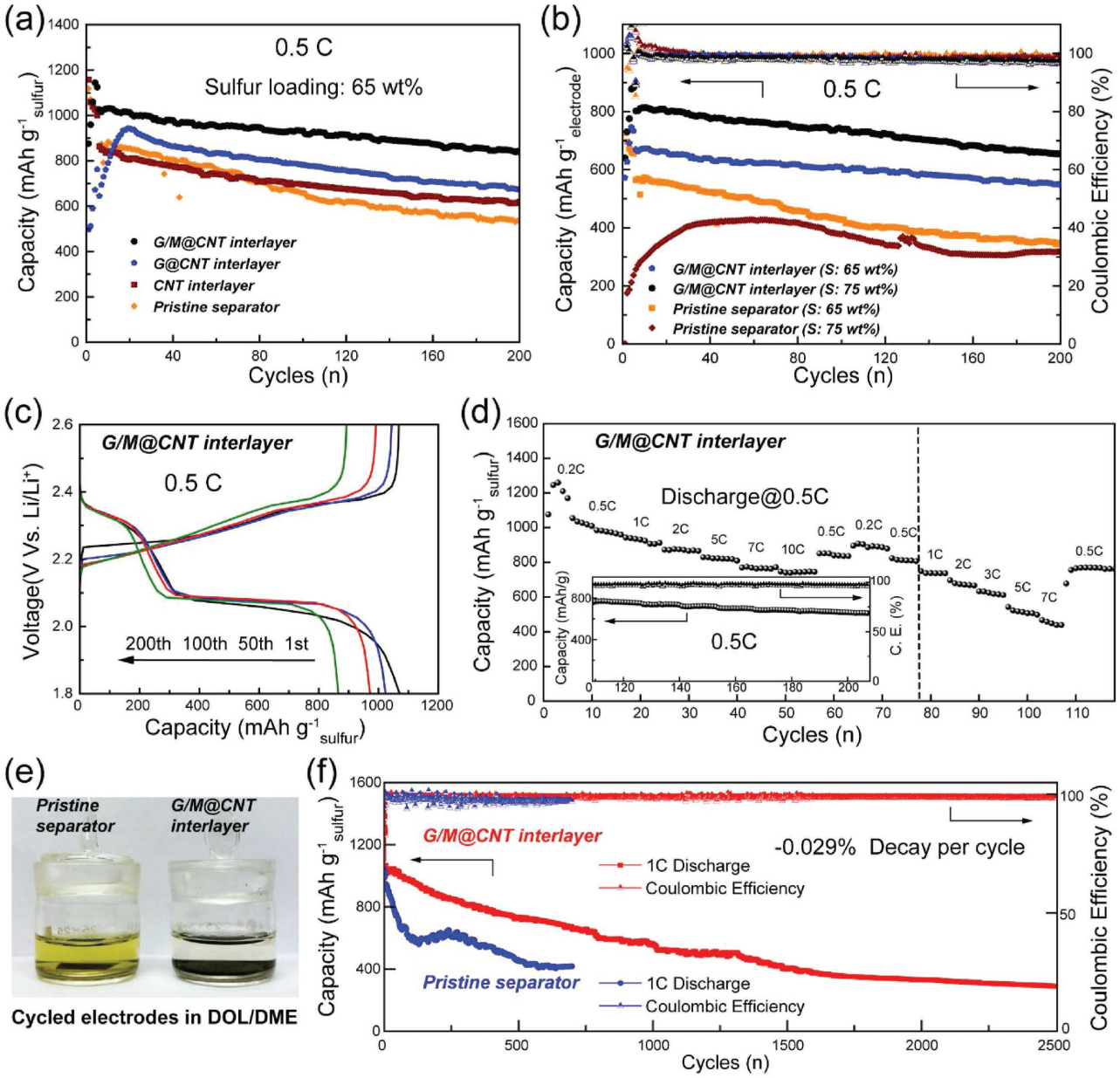

Figure 3. a) Cycling performances of electrodes with the CNT, G@CNT, and G/M@CNT interlayers at 0.5 C. b) Cycling performances of electrodes with/without the G/M@CNT interlayer at various sulfur contents at 0.5 C. c) Charge/discharge voltage profiles of electrode with the G/M@CNT interlayer at 1st, 50th, 100th, and 200th cycles. d) Rate performances of electrode with the G/M@CNT interlayer, and postcycling test at 0.5 C (inset). e) Photographs of cycled electrodes with/without the G/M@CNT interlayer in DOL/DME solution. f) Prolonged cycling performances of electrodes with/without the G/M@CNT interlayer at 1 C.

with G@CNT, G/M@CNT (MnO_2 2 wt%), and G/M@CNT (MnO_2 5 wt%) interlayers. With the addition of 2 wt% MnO_2, the cycling performance was obviously promoted. However, as the content of MnO_2 increased to 5 wt%, the electrode demonstrated decreased capacity and lower coulombic efficiency at ≈90%–92%. The MnO_2/CNT electrode showed a charge voltage plateau at 2.10 V (Figure S4b, Supporting Information), and the side reaction in the voltage window from 1.80 to 2.60 V had a negative effect on the coulombic efficiency of the Li–S cell. Since MnO_2 had a double-edged effect on improving the cycling stability by polysulfide trapping and decreasing the coulombic efficiency due to side reaction, the addition of MnO_2 should be optimized. In this study, the content of MnO_2 nanoparticles in the interlayer was ≈0.05 mg cm^{-2} (2 wt%).

Figure 3b shows the cycling performances of electrodes (various sulfur contents) with the G/M@CNT interlayer and the pristine separator at 0.5 C. The cells with the pristine separator and sulfur contents of 65 and 75 wt% showed capacities of only 568 and less than 200 mA h $g^{-1}_{electrode}$, respectively, based on the weight of the whole electrode, along with fast capacity

decay. In contrast, the cells with the G/M@CNT interlayer and sulfur contents of 65 and 75 wt% showed capacities of 670 and 813 mA h $g^{-1}_{electrode}$, respectively, after activation, and had outstanding cycling stabilities with capacity retentions of 81.4% and 80.4% after 200 cycles. Even when the sulfur content was increased to 80 wt%, the cell with the G/M@CNT interlayer showed a capacity of up to 620 mA h $g^{-1}_{electrode}$ after electrochemical activation (Figure S5, Supporting Information), much higher than that with the pristine separator.

It should be noted that the electrochemical performances of the cells were affected by the number of vein–membrane films in the G/M@CNT interlayer. Figure S6 (Supporting Information) shows the cycling performances of cells with the pristine separator, and the G/M@CNT interlayer with 5 and 10 layers of the vein–membrane hybrid film. The electrochemical properties of the cells improved greatly compared with that of the pristine separator when the number of vein–membrane films in the G/M@CNT functional interlayer was increased to 5 and 10. A thicker G/M@CNT functional interlayer would result in better cycling performances. However, the energy densities of the cells decreased as the interlayer became thicker, therefore a G/M@CNT interlayer with 10 layers of the vein–membrane hybrid film was optimum in this study. When a separator coated with an ultrathin G/M@CNT interlayer was applied, capacity fading originating from the shuttle effect was greatly suppressed, showing the vital role of the vein–membrane sandwich structure of the G/M@CNT interlayer in improving the electrochemical performances of Li–S batteries.

High sulfur loading is also essential in developing high-performance Li–S batteries. The sulfur loading in the cathode should be at least 70 wt% to obtain Li–S batteries with high volumetric energy densities.[45] Great efforts have been made to achieve high sulfur loadings.[46–48] However, in these previous studies, the active sulfur materials were generally mixed with a conductive additive and a polymer binder, and then pasted on Al current collector (areal density 4.10 mg cm^{-2} and thickness 20 μm). Addition of these inactive materials reduces the energy density of the electrode. In this work, freestanding S–CNT composite electrodes were developed. Because SACNTs have excellent conductivity and mechanical properties, there was no need to use an additional conductive agent, polymer binder, or current collector. The sulfur contents reached 60–80 wt%. Consequently, the energy densities of the cells greatly increased. The electrochemical performances of the sulfur-rich electrodes were further improved by the functional G/M@CNT interlayer.

The charge/discharge voltage profiles of the electrode with a sulfur content of 75 wt% and a G/M@CNT interlayer in the 1st, 50th, 100th, and 200th cycles are shown in Figure 3c. Two typical discharge plateaus are observed, corresponding to two electrochemical processes. The higher discharge voltage plateau, at 2.35 V, indicates reduction of elemental S to Li_2S_8; the corresponding discharge capacity (Q_H) is often used to evaluate the extent of polysulfide generation and the polysulfide-trapping capabilities of cells.[4,33,49] The Q_H in the 200th cycle was 90.1% of that in the first cycle, indicating that loss of active sulfur was greatly suppressed by the G/M@CNT interlayer. The lower discharge voltage plateau, at 2.11 V, represents the conversion of polysulfides to Li_2S_2/Li_2S, which contributes to the main discharge capacity (≈80%) of a Li–S cell. The smooth and well-overlapped discharge plateaus for 200 cycles show that the solid-state redox reaction has stable reversibility, despite the insolubility and low Li-ion diffusivity of Li_2S_2/Li_2S. This is ascribed to the high polysulfide-trapping ability of the MnO_2 nanoparticles and GO sheets, and the excellent conductivity of the cross-stacked SACNT films.

Electrodes with the G/M@CNT interlayer gave excellent rate performances because of the synergetic effect of the sandwiched vein–membrane structure. Figure 3d shows that at a constant discharge rate of 0.5 C for the first 77 cycles, the electrodes had high reversible discharge capacities of 1259, 1055, 960, 829, and 747 mA h g^{-1} at corresponding charge rates of 0.2, 0.5, 1, 5, and 10 C. After the high-rate test, the electrode was recycled at 0.2 C, and a reversible capacity of 908 mA h g^{-1} was still obtained. The corresponding voltage profiles at different charge rates are shown in Figure S7 (Supporting Information). Although the polarized charge voltage plateaus increased at high charge currents, the electrode still showed favorable reversibility. The cell was then examined at stepwise charge/discharge rates from 1 to 7 C, and capacities of 543 and 498 mA h g^{-1} were obtained at charge/discharge rates of 5 and 7 C, respectively. The corresponding voltage profiles are shown in Figure S8 (Supporting Information). The discharge voltage plateaus descended with increasing charge/discharge rate. After the series of high-rate tests, the electrode was used for 100 cycles at 0.5 C (inset of Figure 3d); it showed good cycling stability, with the capacity remaining at around 800 mA h g^{-1}, and a coulombic efficiency of almost 100%. Even at a charge rate as high as 25 C, corresponding to a charge duration of less than 40 s and a charge current up to 40 A g^{-1}, the electrode showed a reversible capacity of 535 mA h g^{-1} (Figure S9, Supporting Information). The electrode was then cycled at 0.2 C and delivered a capacity of 993 mA h g^{-1}. In contrast, the electrode with the pristine separator failed at a charge rate of 5 C.

The excellent cycling stabilities and rate performances of the electrodes with the G/M@CNT interlayer arose from three factors. First, the MnO_2 nanoparticles and GO sheets played important roles in restricting polysulfides diffusion by strong interactions with the polysulfides and subsequent chemical adsorption. Second, the sandwiched vein–membrane structure provided an effective physical shield with reduced pore sizes to restrain the polysulfides. Third, efficient electron transfer is beneficial for the surface reaction between polysulfides and oxygen groups and the resulting polysulfide adsorption.[36,38,39] Therefore, the highly conductive CNT network in the sandwiched vein–membrane interlayer could greatly accelerate this adsorption process and to enhance the polysulfide trapping ability of the interlayer.

As shown in Figure 3e and Figure S10 (Supporting Information), the detached cells (after 200 cycles at 0.2 C) with and without the G/M@CNT interlayer were compared by soaking the electrodes in dioxolane (DOL)/dimethoxyethane (DME) solution. The solution containing the electrode with the G/M@CNT interlayer (right) was much clearer than that with the pristine separator (left), confirming that most polysulfides had been reduced to insoluble sulfur confined in the electrode. Even if there existed few dissolved polysulfides, the G/M@CNT interlayer had completely adsorbed them, restraining their dissolution into the DOL/DME solution.

The functional G/M@CNT interlayer also contributed to the significantly prolonged cycling stability of the S–CNT electrode. As shown in Figure 3f, at a charge/discharge rate of 1 C, the S–CNT electrode with a G/M@CNT interlayer gave an excellent long-life performance for over 2500 cycles. A reversible capacity of 293 mA h g^{-1} was obtained in the 2500th cycle, with an average capacity decay as low as –0.029% per cycle. The coulombic efficiency remained at 98.8%. The shuttle factor f is used to evaluate the extent of the shuttle effect.[50] As previously reported, because of a severe shuttle effect, carbon/sulfur composite electrodes often have low coulombic efficiencies, i.e., less than 90%, and large shuttle factors ($f > 0.3$).[5,14,15] In this work, the electrode had a much lower shuttle factor ($f \approx 0.036$) because of the excellent polysulfide-trapping ability of the G/M@CNT interlayer. The electrode with the pristine separator gave an inferior performance and failed at the 700th cycle.

Glass cells were used to visually examine the polysulfide-trapping ability of the G/M@CNT interlayer in the Li–S cell (**Figure 4**). The left chamber was filled with DOL/DME solvent containing polysulfides (Li_2S_6), and the right chamber was filled with pure DOL/DME solvent. These two chambers were separated by the pristine separator (top row) and the G/M@CNT-interlayer-coated separator (bottom row). The pure DOL/DME solvent (right) changed from colorless to yellow–brown after 24 h, showing rapid diffusion of polysulfides through the pristine separator. In comparison, little color change was observed in the right chamber of the glass cell with the G/M@CNT-interlayer-coated separator, indicating that polysulfides diffusion was significantly suppressed by the ultrathin G/M@CNT interlayer. Surface morphologies of the GO@CNT and MnO_2@CNT interlayers are shown in Figure S11 (Supporting Information) and their polysulfide-trapping abilities were also tested using glass cells. Although MnO_2 nanoparticles showed slightly better polysulfide-adsorption ability than GO sheet,[38] the relatively porous structure of the CNT networks could not restrain them all (Figure S11b, Supporting Information). In contrast, GO sheets could effectively cover the open structure of the stacked CNT network. As a result, less color change was observed in the right chamber of the glass cell with the GO@CNT interlayer, demonstrating its better polysulfide trapping ability than the MnO_2@CNT interlayer (Figure S11c,d, Supporting Information). These results suggested that GO sheets, MnO_2 nanoparticles, and the CNT network functioned together in the G/M@CNT interlayer: the CNT network provided structural support and conductive pathways, and GO sheets covered the open structure of the CNT network, and MnO_2 nanoparticles provided further polysulfide adsorption sites.

The G/M@CNT interlayer also contributed to a notable improvement in the self-discharge behavior of the Li–S cell. **Figure 5**a shows the open-circuit voltage profiles of electrodes with the G/M@CNT interlayer and the pristine separator. The electrode with the pristine separator showed voltage fluctuations during a resting period from 30 to 180 h. Because of dissolution of active sulfur during long-term resting, the conventional Li–S cell with the pristine separator showed severe self-discharge behavior, which led to capacity decay. However, for the electrode with the G/M@CNT interlayer, the process was smooth, without any self-discharge behavior during the entire resting time. Figure 5b shows typical charge/discharge voltage profiles of the electrodes at 0.5 C after 20 d rest. For the electrode with the G/M@CNT interlayer, the voltage plateau was almost unchanged compared with that of the fresh cell (Figure 3c), and the voltage hysteresis was only 0.169 V, indicating that the electrode had outstanding redox kinetics. In contrast, because of the continuous loss of active sulfur during the resting period, the electrode with the pristine separator showed severe polarization, with an unstable voltage plateau at around 1.90 V, and the voltage hysteresis increased to 0.409 V. Figure 5c,d shows the cycling performances of the electrodes after 20 d rest. As shown in Figure 5c, the poor polysulfide-trapping ability of the pristine separator led to severe self-discharge behavior, resulting in an initial capacity retention of only 25.8%. It should be noted that there was an increasing

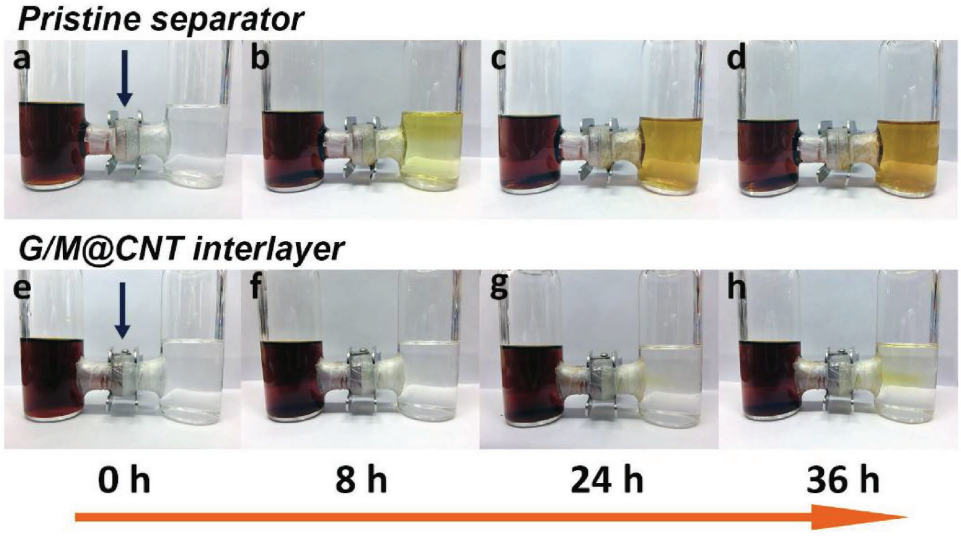

Figure 4. Photographs of glass cells with polysulfides (Li_2S_6) in DOL/DME solution and pure DOL/DME solvent in left and right chambers, respectively, separated by pristine separator (top row) and the G/M@CNT interlayer coated separator (bottom row).

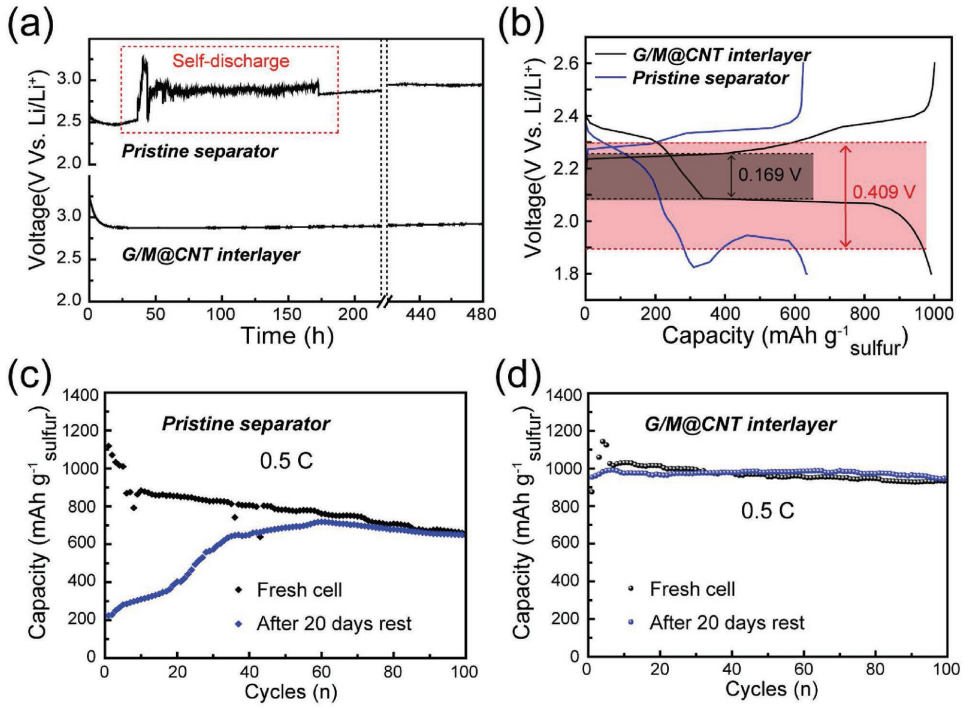

Figure 5. Self-discharge behaviors of electrodes with/without the G/M@CNT interlayer. a) Open-circuit voltage profiles showing self-discharge behaviors. b) Charge/discharge voltage profiles of electrodes with/without the G/M@CNT interlayer at 0.5 C after 20 d rest. Cycling performances of electrodes with c) pristine separator, and d) the G/M@CNT interlayer at 0.5 C after 20 d rest.

tendency of the discharge capacities during the first 50 cycles; the corresponding charge/discharge voltage profiles are shown in Figure S12 (Supporting Information). Due to the self-discharge behavior resulted from polysulfides dissolution and the low conductivity of Li_2S_2/Li_2S, the electrode exhibited inferior reaction kinetics and a relatively long activation process was needed to obtain a stable discharge voltage plateau.[4,5] In contrast, the electrode with the G/M@CNT interlayer had excellent stability with a high initial capacity retention of 93.0% after 20 d rest compared with that of the fresh cell (Figure 5d). The capacity retention after 100 cycles at 0.5 C was 99.4%, retaining a capacity of ≈950 mA h g^{-1}. Figure S13 (Supporting Information) shows the corresponding charge/discharge voltage profiles of the electrode with the G/M@CNT interlayer tested after 20 d rest. The well-overlapped charge/discharge voltage profiles show the excellent polysulfide-trapping ability and cycling stability endowed by the G/M@CNT interlayer. An activation process was observed for the first 10 cycles. However, this process was much shorter than in the case of the electrode with the pristine separator because of the ability of the G/M@CNT interlayer to suppress self-discharge and the excellent conductivity of the cross-stacked SACNT films.

Figure 6 shows SEM images of the Li anodes of the cycled Li–S batteries with/without the G/M@CNT interlayer. Previous studies showed that the solid electrolyte interface film on the Li anode in a Li–S battery differs from that in a conventional LIB because of the dissolved polysulfides. The passivation layer formed on the Li anode surface in an Li–S batteries consists of the reaction products from lithium polysulfides and electrolyte additive.[8,51,52] The shuttled polysulfides react with the Li anode and electrolyte additive, leading to a thicker passivation layer on the Li anode. The side reaction results in a higher inner resistance, and rapid capacity decay because of continuous loss of

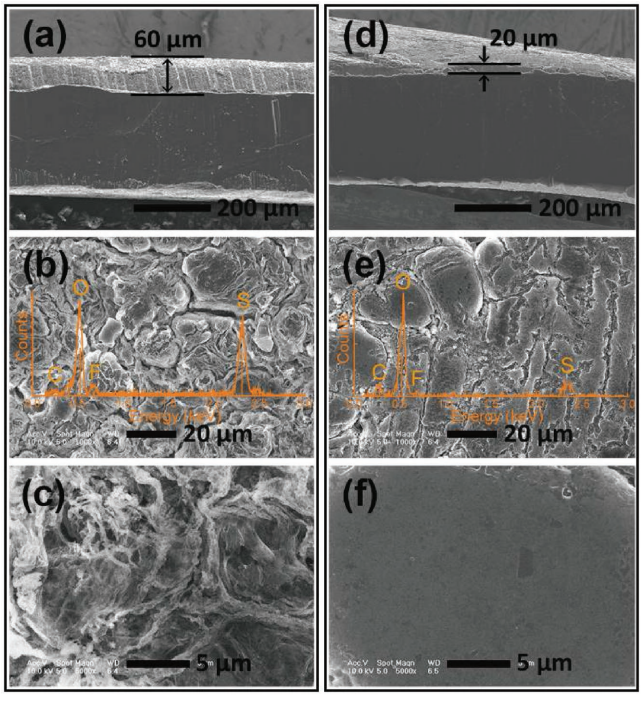

Figure 6. SEM images and EDX spectra for cycled Li anodes in cells with a–c) the pristine separator, and d–f) the G/M@CNT interlayer.

active sulfur and electrolyte. As shown in Figure 6a, the cross-sectional SEM image of the cycled Li anode of the cell with the pristine separator had a thick passivation layer (≈60 µm). The surface morphology (Figure 6b,c) was rough, and the EDX spectrum (inset of Figure 6b) indicates high sulfur content, which originated from the complex passivation layer. The passivation layer of the cycled Li anode of the cell with the G/M@CNT interlayer was much thinner (≈20 µm), as shown in Figure 6d. The surface (Figure 6e,f) was smooth, and the EDX spectrum shows low sulfur content. These results indicate that the shuttle effect and side reactions were greatly suppressed by the G/M@CNT interlayer.

The cyclic voltammetry (CV) profiles of the electrode with the G/M@CNT interlayer in the first and second cycles are shown in **Figure 7**a. In the cathodic scan, two reduction peaks occurred, at 2.32 and 2.03 V, corresponding to the conversion of cyclo-S_8 to high-order lithium polysulfides, and further reduction to lithium sulfides (Li_2S_2/Li_2S), respectively. The two oxidation peaks in the anodic scan are assigned to the reverse reactions: the formation of Li_2S_x and cyclo-S_8 at 2.31 and 2.40 V, respectively.[5,6] The sharp and symmetric redox peaks in CV curves indicated fast electrochemical kinetics endowed by the G/M@CNT interlayer, and the overlapping of the positions and magnitudes of the redox peaks demonstrated good electrochemical reversibility. The hysteresis of the corresponding redox peaks was only 0.288 V, indicating little polarization of the electrode. An oxidation shoulder was observed at ≈2.45 V and decreased in the following cycle. The small shoulder in the CV curve (Figure 7a) was not obviously reflected in the voltage profiles (Figure 3c). Based on the electrochemical impedance spectroscopy (EIS) analysis below, along with other related works,[36–39] the small shoulder was ascribed to the electrochemical conversion from the surface-bound intermediates ($S_2O_3^{2-}$) and polysulfides to cyclo-S_8. Because this intermediate reaction occurred very closely to the polysulfide conversion (Figure 7c), a small oxidization shoulder was observed in the precise CV test, whereas no evidence was reflected in the voltage profiles performed by the galvanostatic test. The cell with the pristine separator suffered from severe polysulfide shuttling, resulting in hysteresis of the redox peaks as large as 0.391 V and an inferior electrochemical performance (Figure S14, Supporting Information).

An EIS study was performed on the Li–S cells with/without the G/M@CNT interlayer (Figure 7c,d). A typical discharge voltage profile of the sulfur cathode at 0.1 C is presented in Figure 7b; it shows two voltage plateaus, as discussed before. Nyquist plots at frequencies ranging from 100 kHz to 100 mHz were obtained at various discharge stages, corresponding to those marked in Figure 7b. The first discharge process, from point A (2.38 V) to points B and C (2.13 V), corresponds to conversion of S_8 to soluble polysulfides, and the second discharge process, from point C (2.13 V) to points D, E, and F (1.80 V), corresponds to further nucleation to Li_2S_2/Li_2S.[4,5] It has been suggested that the semicircles in the high-frequency and

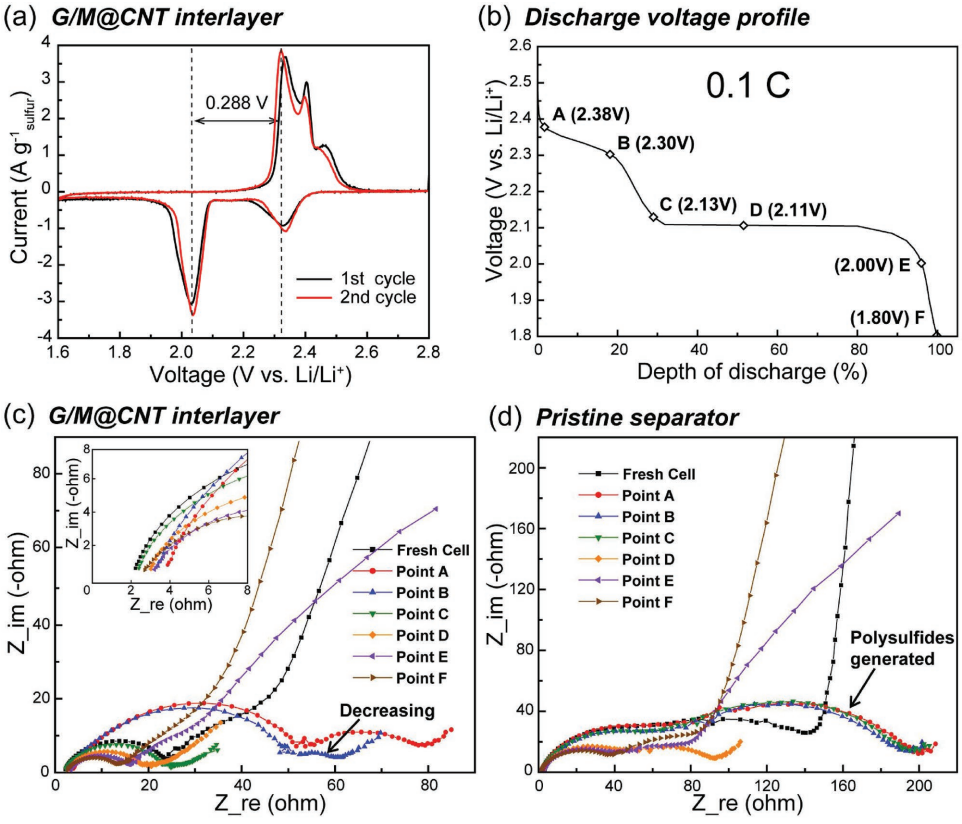

Figure 7. a) CV profiles of electrode with the G/M@CNT interlayer. b) Typical charge/discharge voltage profiles at 0.1 C, marked at different stages in EIS tests. EIS results at different discharge depths of electrodes with c) the G/M@CNT interlayer and d) pristine separator.

middle-frequency (MF) regions were related to charge-transfer resistance and the formation of a solid film of Li_2S and Li_2S_2, respectively.[53,54] However, other literatures, together with the results discussed below, suggest that the MF semicircles were caused by polysulfide generation, and the inclined line in the low-frequency region was strongly related to inner diffusion.[55,56] The depressed semicircle in Figure 7c for the fresh cell (black line) indicates that the charge-transfer resistance (R_{ct}) and ohmic resistance of the electrode with the G/M@CNT interlayer were about 21 and 2.2 Ω, respectively. As the electrode was discharged to point A (2.38 V, red line), where polysulfides generation began, a depressed semicircle appeared in the MF region and the ohmic resistance increased slightly (inset of Figure 7c) because of the increased electrolyte resistance from the soluble polysulfides. As the electrode was further discharged to point B (2.30 V, blue line), the second semicircle decreased significantly, although the amount of polysulfides was expected to increase, and the electrolyte resistance decreased slightly, as indicated by the ohmic resistance (inset of Figure 7c). As the electrode was discharged to point C (2.13 V), where the amount of soluble polysulfides should reach a maximum, the MF depressed semicircle disappeared, with an R_{ct} of only 22 Ω. These results suggest that polysulfide generation was suppressed by the G/M@CNT interlayer and was restricted during the discharge process. The R_{ct} of the electrode with the G/M@CNT interlayer decreased continuously to as low as 11 Ω; this is mainly ascribed to the high conductivity of the cross-stacked SACNTs in the G/M@CNT interlayer. The slope of the inclined line in the low-frequency region in the discharged state (point F, brown line) was the same as that for the fresh cell, confirming significant suppression of polysulfides dissolution in the electrolyte by the G/M@CNT interlayer. In contrast, as shown in Figure 7d, for the electrode with the pristine separator, the initial R_{ct} was around 80 Ω (black line), and a depressed semicircle appeared in the MF region because of the self-discharge behavior shown in Figure 5a. The size of the MF depressed semicircle then increased until the cell was discharged at point C. These results suggest polysulfides dissolution into the electrolyte. The slope of the inclined line at point F was smaller than that for the fresh cell (Figure 7d), indicating increased electrolyte resistance because of polysulfides generation and dissolution.

Table 1 summarizes the electrochemical performance of the Li–S batteries improved by the G/M@CNT interlayer, and other types of interlayers reported in literature. The electrode with the G/M@CNT interlayer has many distinctive properties, including a low areal density (0.104 mg cm^{-2}), high sulfur content (60–80 wt%), long-term cycling stability (–0.029% decay per cycle for 2500 cycles), and a high rate performance (747 mA h g^{-1} at 10 C). Moreover, the S–CNT electrodes in this study do not require a binder or current collector. The significant improvements on the cycling stability, rate performance, anti-self-discharge, and energy densities of Li–S cells originated from the following aspects: (1) The CNT network provided effective support veins for the hybrid interlayer, GO sheets acted as both support membrane for MnO_2 dispersion and physical shield against the polysulfides diffusion. Thus, the sandwiched vein–membrane interlayer exhibited high flexibility and low areal density. (2) In the G/M@CNT interlayer, GO/MnO_2 showed effective adsorption capability due to the intermediate surface reaction between their oxygen groups and polysulfides.[32,38] The highly conductive CNT network is beneficial for charge transfer during the surface reaction and thus can further accelerate the adsorption process. (3) MnO_2 provided more adsorption sites for polysulfides; GO sheets served as a physical membrane to cover the open structure of the stacked CNT networks for polysulfide trapping.

3. Conclusion

In summary, an ultrathin functional G/M@CNT interlayer was designed as an efficient polysulfide-trapping shield for high-performance Li–S batteries. The interlayer benefited from the excellent mechanical properties and high conductivity of SACNTs and had an ultrathin sandwiched and conductive vein–membrane structure composed of MnO_2 nanoparticles, GO sheets, and cross-stacked SACNT films. The G/M@CNT interlayer provided a physical shield against polysulfides diffusion through the vein–membrane films, and enabled chemical adsorption and confinement of polysulfides by the oxygen groups of the MnO_2 nanoparticles and GO sheets. The sulfur electrode with the G/M@CNT interlayer showed excellent cycling stability, with capacity decay of –0.029% per cycle for 2500 charge/discharge cycles at 1 C. A high rate performance was also achieved, with a capacity of 747 mA h g^{-1} at a charge rate of 10 C. Improved by the G/M@CNT interlayer, the S–CNT composite electrodes with high sulfur loading ranging from 60 to 80 wt%, presented high discharge capacity of 813 mA h $g^{-1}_{electrode}$ at 0.5 C based on the weight of the whole

Table 1. Electrochemical properties of various functional interlayers in Li–S batteries.

Description	Areal density	S content [wt%]	Capacity decay [% per cycle]	High rate performance	Binder/current collector free	References
GO/MnO_2@CNT	0.104 mg cm^{-2} (4.7 wt%)	60–80	–0.029% @1C (2500th)	747 mAh g^{-1} (10 C)	Yes	This work
Polypyrrole nanotube film	1 mg cm^{-2}	80	–0.118% @C/2 (300th)	–	No	[27]
Nafion	0.7 mg cm^{-2}	50	–0.08% @1C (500th)	533 mAh g^{-1} (5 C)	No	[28]
Carbon	0.5 mg cm^{-2}	60–70	–0.09% @C/2 (500th)	–	No	[29]
MWCNT	0.17 mg cm^{-2}	70	–0.14% @1C (300th)	–	No	[31]
GO	0.12 mg cm^{-2}	63	–0.23% @C/10 (100th)	570 mAh g^{-1} (2 C)	No	[32]
TiO_2/graphene	7.8 wt%	51.2	–0.01% @2C (1000th)	630 mAh g^{-1} (3 C)	No	[33]

electrode, and the capacity retention was 80.4% after 200 cycles. After 20 d rest, the cell with the G/M@CNT interlayer showed a low self-discharge rate, with 93.0% capacity retention compared with the fresh cell, along with excellent redox kinetics. The S–CNT composite electrodes were fabricated using a simple dispersion and codeposition method, without binder or current collector, and the obtained electrodes exhibited high flexibility. Large-scale fabrication of the G/M@CNT interlayer via layer-by-layer stacking of the vein–membrane hybrid film is feasible. Therefore, the strategy of using the G/M@CNT interlayer as a polysulfide-trapping shield has great potential in commercial applications of high-performance Li–S batteries.

4. Experimental Section

Fabrication of SACNT Arrays and G/M@CNT Interlayer: SACNT arrays of diameter 10–20 nm and height 300 µm were synthesized on silicon wafers by chemical vapor deposition with iron as the catalyst and acetylene as the precursor. Details of the synthetic procedure can be found in previous papers.[22–24] Continuous SACNT films were drawn from the SACNT arrays using an end-to-end joining mechanism. MnO_2 nanoparticles (5 mg; Alfa Aesar) and GO sheets (5 mg; XF Nano Inc., China) were dispersed in ethanol (60 mL) by intensive ultrasonication for 30 min. A polypropylene film (Celgard 2400) was fixed on a flat glass and covered with one layer of the cross-stacked SACNT film. The mixture of uniformly dispersed MnO_2 nanoparticles and GO sheets was then deposited on the cross-stacked SACNT film. The alcohol was evaporated to give a vein–membrane film constructed from the MnO_2 nanoparticles, GO sheets, and cross-stacked SACNT film. This procedure was repeated to give sandwiched vein–membrane films with 5 or 10 cross-layered structures (G/M@CNT interlayer). The contents of both MnO_2 nanoparticles and GO sheets for the 10 cross-layered G/M@CNT interlayer were 0.05 mg cm^{-2}. Finally, a G/M@CNT interlayer- coated separator was punched into circles of diameter 19 mm.

Fabrication of S–CNT Composite Electrodes: SACNTs were oxidized in a mixed solution of HNO_3/H_2SO_4 (3:1 weight ratio) at 80 °C for 4 h to obtain oxidized CNTs (oCNTs). Sulfur powder (Beijing Dk Nano Technology Co., Ltd) and oCNTs were well dispersed in water/ethanol solution by intensive ultrasonication (1000 W) for 30 min. A binder-free and flexible S–CNT film with a uniform dispersion of sulfur nanoparticles on oCNTs was obtained by vacuum infiltration and drying at 50 °C. The S–CNT film was sealed in a steel container and heat-treated at 155 °C for 8 h. The S–CNT composite electrodes had various sulfur loadings, ranging from 60 to 80 wt%, corresponding to areal sulfur densities of 1.11 to 2.37 mg cm^{-2}.

Characterization: TGA was conducted (Pyris 1 TGA, PerkinElmer, USA) at a heating rate of 10 °C min^{-1} in air from 25 to 500 °C. The morphologies and structures of the G/M@CNT interlayers and S–CNT composite electrodes were investigated using SEM (Sirion 200, FEI) and transition electron microscopy (TEM; Tecnai G2F20, FEI). Coin-type (CR 2016) half-cells with an S–CNT composite as the working electrode and pure Li foil as the reference electrode were assembled in a glove box filled with protective argon gas (M. Braun Inert Gas Systems Co., Ltd., Germany). A G/M@CNT-interlayer-coated polypropylene film (Celgard 2400) was used as a separator, with the G/M@CNT interlayer adjacent to the S–CNT composite cathode. A 1 M lithium bis(trifluoromethanesulfonyl)imide (LiTFSI) solution in DOL and DME (volume ratio 1:1) with 0.2 M $LiNO_3$ was used as the electrolyte. Visual examination of the polysulfide-trapping effect of the G/M@CNT interlayer was performed using an H-type glass cell, in which the left chamber was filled with 0.05 M Li_2S_6 in DOL/DME solution, and the right chamber was filled with pure DOL/DME solvent. CV and EIS were performed using a potentiostat/galvanostat (Princeton PARStat 2273). Charge/discharge measurements were performed using a Land battery test system (Wuhan Land Electronic Co., China) in the voltage window 1.8–2.6 V at various charge/discharge rates at room temperature.

Calculation of Shuttle Factor: The shuttle factor, which reflects the extent of the shuttle effect, was suggested by Mikhaylik and Akridge[50]

$$f = k_s Q_H [S_{total}]/I \quad (1)$$

where k_s is the heterogeneous reaction constant related to polysulfides diffusion and reaction, Q_H is the theoretical charge/discharge capacity of the high plateau, and I is the charge/discharge current. Based on previous papers,[50,57] the relationship between the coulombic efficiency (C_{eff}) and the shuttle factor f can be expressed as

$$C_{eff} = \frac{2+(\ln(1+f))/f}{2-(\ln(1-f))/f} \quad (2)$$

Supporting Information

Supporting Information is available from the Wiley Online Library or from the author.

Acknowledgements

This work was supported by NSFC (51472141) and the National Basic Research Program of China (2012CB932301).

Received: December 17, 2016
Revised: February 14, 2017
Published online: March 24, 2017

[1] N. Nitta, F. Wu, J. T. Lee, G. Yushin, *Mater. Today* **2015**, *18*, 252.
[2] B. Scrosati, J. Garche, *J. Power Sources* **2010**, *195*, 2419.
[3] P. G. Bruce, S. A. Freunberger, L. J. Hardwick, J.-M. Tarascon, *Nat. Mater.* **2012**, *11*, 172.
[4] X. Ji, L. F. Nazar, *J. Mater. Chem.* **2010**, *20*, 9821.
[5] A. Manthiram, Y. Fu, S. Chung, C. Zu, Y. Su, *Chem. Rev.* **2014**, *114*, 11751.
[6] A. Rosenman, E. Markevich, G. Salitra, D. Aurbach, A. Garsuch, F. F. Chesneau, *Adv. Energy Mater.* **2015**, *5*, 1500212.
[7] W. Y. Li, G. Y. Zheng, Y. Yang, Z. W. Seh, N. Liu, Y. Cui, *Proc. Natl. Acad. Sci. USA* **2013**, *110*, 7148.
[8] G. Zhou, Y. Zhao, A. Manthiram, *Adv. Energy Mater.* **2015**, *5*, 1402263.
[9] W. D. Zhou, Y. C. Yu, H. Chen, F. J. DiSalvo, H. D. Abruña, *J. Am. Chem. Soc.* **2013**, *135*, 16736.
[10] Z. W. Seh, W. Li, J. J. Cha, G. Zheng, Y. Yang, M. T. McDowell, P. C. Hsu, Y. Cui, *Nat. Commun.* **2013**, *4*, 1331.
[11] L. Qie, A. Manthiram, *Adv. Mater.* **2015**, *27*, 1694.
[12] G. Zhou, S. Pei, L. Li, D. Wang, S. Wang, K. Huang, L. Yin, F. Li, H. M. Cheng, *Adv. Mater.* **2014**, *26*, 625.
[13] W. B. Kong, L. Sun, Y. Wu, K. L. Jiang, Q. Q. Li, J. P. Wang, S. S. Fan, *Carbon* **2016**, *96*, 1053.
[14] H. L. Wang, Y. Yang, Y. Y. Liang, J. T. Robinson, Y. G. Li, A. Jackson, Y. Cui, H. J. Dai, *Nano Lett.* **2011**, *11*, 2644.
[15] J. Guo, Y. Xu, C. Wang, *Nano Lett.* **2011**, *11*, 4288.
[16] K. Jin, X. Zhou, L. Zhang, X. Xin, G. Wang, Z. Liu, *J. Phys. Chem. C* **2013**, *117*, 21112.
[17] L. Sun, M. Y. Li, Y. Jiang, W. B. Kong, K. L. Jiang, J. P. Wang, S. S. Fan, *Nano Lett.* **2014**, *14*, 4044.
[18] L. Sun, W. Kong, Y. Jiang, H. Wu, K. Jiang, J. Wang, S. Fan, *J. Mater. Chem. A* **2015**, *3*, 5305.
[19] S. Lu, Y. Cheng, X. Wu, J. Liu, *Nano Lett.* **2013**, *13*, 2485.

[20] Y. S. Su, Y. Fu, A. Manthiram, *Phys. Chem. Chem. Phys.* **2012**, *14*, 14495.
[21] J. Song, Z. Yu, T. Xu, S. Chen, H. Sohn, M. Regula, D. Wang, *J. Mater. Chem. A* **2014**, *2*, 8623.
[22] K. L. Jiang, Q. Q. Li, S. S. Fan, *Nature* **2002**, *419*, 801.
[23] K. Liu, Y. H. Sun, L. Chen, C. Feng, X. F. Feng, K. L. Jiang, Y. G. Zhao, S. S. Fan, *Nano Lett.* **2008**, *8*, 700.
[24] K. Liu, K. L. Jiang, Y. Wei, S. P. Ge, P. Liu, S. S. Fan, *Adv. Mater.* **2007**, *19*, 975.
[25] P. Arora, Z. M. Zhang, *Chem. Rev.* **2004**, *104*, 4419.
[26] J. Huang, Q. Zhang, F. Wei, *Energy Storage Mater.* **2015**, *1*, 127.
[27] G. Ma, Z. Wen, Q. Wang, C. Shen, P. Peng, J. Jin, X. Wu, *J. Power Sources* **2015**, *273*, 511.
[28] J. Huang, Q. Zhang, H. Peng, X. Liu, W. Qian, F. Wei, *Energy Environ. Sci.* **2014**, *7*, 347.
[29] H. Yao, K. Yan, W. Li, G. Zheng, D. Kong, Z. W. Seh, V. K. Narasimhan, Z. Liang, Y. Cui, *Energy Environ. Sci.* **2014**, *7*, 3381.
[30] Y. Su, A. Manthiram, *Nat. Commun.* **2012**, *3*, 1166.
[31] S.-H. Chung, A. Manthiram, *J. Phys. Chem. Lett.* **2014**, *5*, 1978.
[32] J. Huang, T. Zhuang, Q. Zhang, H. Peng, C. Chen, F. Wei, *ACS Nano* **2015**, *9*, 3002.
[33] Z. Xiao, Z. Yang, L. Wang, H. Nie, M. Zhong, Q. Lai, X. Xu, L. Zhang, S. Huang, *Adv. Mater.* **2015**, *27*, 2891.
[34] T. Jeong, Y. H. Moon, H. Chun, H. S. Kim, B. W. Cho, Y. Kim, *Chem. Commun.* **2013**, *49*, 11107.
[35] G. Ma, Z. Wen, Q. Wang, C. Shen, P. Peng, J. Jin, X. Wu, *J. Power Sources* **2015**, *273*, 511.
[36] L. W. Ji, M. M. Rao, H. M. Zheng, L. Zhang, Y. C. Li, W. H. Duan, J. H. Guo, E. J. Cairns, Y. G. Zhang, *J. Am. Chem. Soc.* **2011**, *133*, 18522.
[37] Q. Zhang, Y. Wang, Z. W. Seh, Z. Fu, R. Zhang, Y. Cui, *Nano Lett.* **2015**, *15*, 3780.
[38] X. Liang, C. Hart, Q. Pang, A. Garsuch, T. Weiss, L. F. Nazar, *Nat. Commun.* **2015**, *6*, 5682.
[39] Z. Li, J. Zhang, D. Lou, *Angew. Chem., Int. Ed.* **2015**, *54*, 12886.
[40] J. Zhou, R. Li, X. Fan, Y. Chen, R. Han, W. Li, J. Zheng, B. Wang, X. Li, *Energy Environ. Sci.* **2014**, *7*, 2715.
[41] M. Vijayakumar, N. Govind, E. Walter, S. D. Burton, A. Shukla, A. Devaraj, J. Xiao, J. Liu, C. Wang, A. Karim, S. Thevuthasan, *Phys. Chem. Chem. Phys.* **2014**, *16*, 10923.
[42] A. L. M. Reddy, M. M. Shaijumon, S. R. Gowda, P. M. Ajayan, *Nano Lett.* **2009**, *9*, 1002.
[43] H. Xia, M. Lai, L. Lu, *J. Mater. Chem.* **2010**, *20*, 6896.
[44] M. V. Reddy, G. V. Subba Rao, B. V. R. Chowdari, *Chem. Rev.* **2013**, *113*, 5364.
[45] Y. Yang, G. Zheng, Y. Cui, *Chem. Soc. Rev.* **2013**, *42*, 3018.
[46] Q. Sun, B. He, X. Zhang, A. Lu, *ACS Nano* **2015**, *9*, 8504.
[47] D. Li, F. Han, S. Wang, F. Cheng, Q. Sun, W. C. Li, *ACS Appl. Mater. Interfaces* **2013**, *5*, 2208.
[48] Q. Li, Z. Zhang, Z. Guo, K. Zhang, Y. Lai, J. Li, *J. Power Sources* **2015**, *274*, 338.
[49] Y.-S. Su, Y.-Z. Fu, B.-K. Guo, S. Dai, A. Manthiram, *Chem. Eur. J.* **2013**, *19*, 8621.
[50] Y. V. Mikhaylik, J. R. Akridge, *J. Electrochem. Soc.* **2004**, *151*, A1969.
[51] R. Cao, W. Xu, D. Lv, J. Xiao, J. Zhang, *Adv. Energy Mater.* **2015**, *5*, 1402273.
[52] S. Xiong, K. Xie, Y. Diao, X. Hong, *J. Power Sources* **2014**, *246*, 840.
[53] L. Yuan, X. Qiu, L. Chen, W. Zhu, *J. Power Sources* **2009**, *189*, 127.
[54] M. He, L. X. Yuan, W. X. Zhang, X. L. Hu, Y. H. Huang, *J. Phys. Chem. C* **2011**, *115*, 15703.
[55] V. S. Kolosnitsyn, E. V. Kuzmina, E. V. Karaseva, S. E. Mochalov, *J. Power Sources* **2011**, *196*, 1478.
[56] C. B archasz, J. Leprêtre, F. Alloin, S. Patoux, *J. Power Sources* **2012**, *199*, 322.
[57] J. Huang, Q. Zhang, S. Zhang, X. Liu, W. Zhu, W. Qian, F. Wei, *Carbon* **2013**, *58*, 99.